ACS APPLIED ENERGY MATERIALS
Cite This: ACS Appl. Energy Mater. 2018, 1, 5145−5150
Letter
www.acsaem.org

Transformation of a Cobalt Carbide (Co_3C) Oxygen Evolution Precatalyst

Jun-Hyuk Kim,[†,∥] Kenta Kawashima,[‡,∥] Bryan R. Wygant,[‡] Oluwaniyi Mabayoje,[‡] Yang Liu,[†] Joy H. Wang,[†] and C. Buddie Mullins*[,†,‡,§]

[†]McKetta Department of Chemical Engineering, [‡]Department of Chemistry, and [§]Texas Materials Institute, University of Texas at Austin, Austin, Texas 78712, United States

Supporting Information

ABSTRACT: We report on the fabrication of cobalt carbide (Co_3C) particles via a wet-chemical synthetic procedure and also describe their electrochemical oxidation to amorphous Co oxide particles that can be used as oxygen evolution reaction (OER) catalysts. Metal chalcogenide, carbide, and pnictide materials have been investigated recently, but there is some controversy regarding the composition of the actual electrocatalytic material. Carbides, in particular, have not been heavily studied as OER catalysts, and their catalytic nature is still an open question. In an effort to contribute to the clarification of the catalytic particle composition during OER, we have thoroughly characterized the elemental composition of the cobalt carbide particles at various times during OER testing and found that the particles are first converted to a transitory core−shell structure (Co_3C core−amorphous Co oxide shell) followed by the gradual but complete conversion to an amorphous Co oxide particle during additional electrochemical OER testing. This amorphous Co oxide particle (derived from Co_3C) maintains the shape of the original parent Co_3C particle and exhibits a high electrochemically active surface area (ECSA). Moreover, the amorphous Co oxide particle derived from Co_3C shows a higher geometric OER activity than either commercial Co oxide particles or Co_3C−CoO_x core−shell particles. We also observe that the fully oxidized Co_3C shows the same intrinsic activity as commercial Co oxide particles when normalized by the ECSA. Accordingly, the amorphous Co oxide particles produced from Co_3C possesses a porous nanostructure capable of electrocatalytically oxidizing water within the internal pores of the particles.

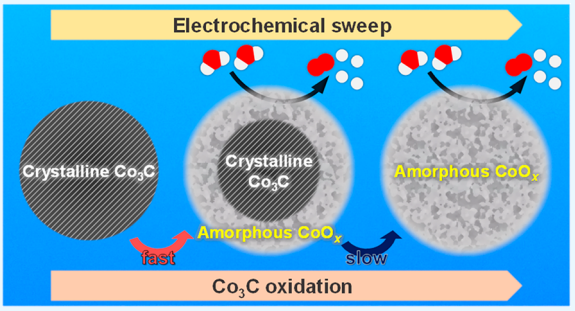

KEYWORDS: *electrocatalyst, energy conversion, oxygen evolution, cobalt carbide, cobalt oxide, precatalyst, electrochemical oxidation*

Hydrogen is a promising energy carrier for the future economy in lieu of the current energy sources that depend on fossil fuels such as coal, oil, and natural gas. When powered by a renewable energy source, water electrolysis could be one of the simplest and most effective methods available for the mass production of hydrogen for energy storage.[1,2] In general, water electrolysis involves the decomposition of water into molecular oxygen (O_2) and hydrogen (H_2). However, the electrochemical reaction for producing O_2 is slower than the H_2 evolution reaction and typically requires more overpotential. Thus, additional research and development will be required to develop electrocatalysts that can overcome the slow reaction kinetics of this reaction.[3]

In recent years, transition metal oxides have been heavily studied as promising oxygen evolution reaction (OER) catalysts.[4,5] Additionally, non-oxide transition metal electrocatalysts (transition metal chalcogenides, phosphides, nitrides, and carbides) have been investigated in alkaline media due to their high earth abundance and low cost.[6−12] However, most non-oxide transition metal electrocatalysts also undergo in situ electrochemical oxidation under OER conditions due to the aqueous and strongly oxidative environments of the OER.[13,14] Therefore, many non-oxide transition metal catalysts will be converted to (oxy)hydroxides at the particle surface[15] to form a core−shell structure (Co_2P [core]−CoO_x [shell],[16] NiSe−-NiOOH,[17] and Co_4N−CoO_x[18]), which frequently show an enhanced OER performance when compared to the native crystalline transition metal oxide (not formed from a non-oxide transition metal precatalyst). The reported final elemental composition and structure of the various precatalyst particles after long-term electrochemical water oxidation testing varies somewhat between these studies, with some accounts describing a core−shell arrangement as the stable final structure of the catalyst and others reporting a uniformly oxidized particle. For example, Chen et al. reported that binary, ternary, and quaternary transition metal (Co, Ni, and Fe) oxides were formed from their parent sulfides during water oxidation.[19] Additionally, Xu et al. reported a highly active bimetallic $Ni_xFe_{1-x}Se_2$ as a "template precursor" which is entirely converted to an amorphous nickel iron oxide during

Received: August 11, 2018
Accepted: October 1, 2018
Published: October 1, 2018

DOI: 10.1021/acsaem.8b01336
ACS Appl. Energy Mater. 2018, 1, 5145−5150

OER operation.[20] Further, Mabayoje et al. also recently reported that amorphous NiO_x particles were uniformly created from NiS "precatalyst" particles during OER testing.[21]

However, other reports have found a stable core−shell arrangement of the materials upon conducting water oxidation experiments. Kwak et al. studied $CoSe_2$ and $NiSe_2$ as bifunctional electrocatalysts for water splitting and reported that both $NiSe_2$ and $CoSe_2$ starting materials transformed into oxyhydroxide outer layers with the parent selenide transition metal material underneath enhancing the electrical conductivity during catalysis.[22] Additionally, Swesi et al. investigated Ni_3Se_2 as a water oxidation electrocatalyst and reported, based on both Raman spectroscopy and X-ray photoelectron spectroscopy, that the Ni_3Se_2 elemental composition was maintained throughout the particle even after extended periods of water oxidation electrocatalysis.[23] Nevertheless, from a thermodynamic point of view one would expect all of the above materials to be precatalysts that eventually convert to metal oxides unless there are structural or kinetic barriers to oxide transformation.[13,14] Studies like those listed above clearly indicate that such barriers against their oxidation must exist, and undoubtedly influence the catalytic performance of these materials. Thus, revealing the time evolution of this class of OER material under highly oxidizing conditions is very important for further development of these earth-abundant, potentially useful materials as well as better understanding of their oxidation mechanism.

Herein we report on the fabrication of cobalt carbide (Co_3C) as a novel precatalyst candidate via wet-chemical synthesis and its transformation (electrochemical oxidation process) under water oxidizing conditions using high-resolution transmission electron microscopy (HRTEM), X-ray photoelectron spectroscopy (XPS), scanning electron microscopy (SEM), X-ray diffraction (XRD), and electrochemically active surface area (ECSA) to carefully characterize the material after various exposures of the Co_3C particles to OER conditions. Here, it should be noted that, until now, researchers have indicated the higher ECSA of oxide samples derived from non-oxide transition metal materials but very few researchers have attempted to answer the question of whether the improved activity of these materials is only as a result of their relatively higher surface areas.[19,21,24] In this study, by normalizing the derived currents by the ECSA of the films, we also attempt to understand if the relatively higher activity of derived Co oxide films is intrinsic. During our OER experiments, the surface of the Co_3C precatalyst particle was initially converted to an amorphous Co oxide while leaving the core of the particle as Co_3C. However, this core−shell structure is transitory and the Co_3C particle is eventually completely transformed into amorphous Co oxide after additional use as a water oxidation electrocatalyst, increasing the effective ECSA. From these experiments, we first show that the carbide is simply a precatalyst precursor for the highly active cobalt oxide OER catalyst with an amorphous nature and a nanoporous structure.

In the XRD patterns (shown in Figure 1a), the Co_3C phase (ICDD PDF No. 043-1144) was observed in our as-prepared Co_xC sample (the sample before heat treatment of Co_3C; synthesis details in the Supporting Information (SI)) with some impurity peaks attributed to surfactant/solvent and a few unknown peaks (details in SI Figure S1). In order to remove the impurities and crystallize the material, we calcined the Co_xC sample for 3 h at 300 °C under Ar flow. The XRD

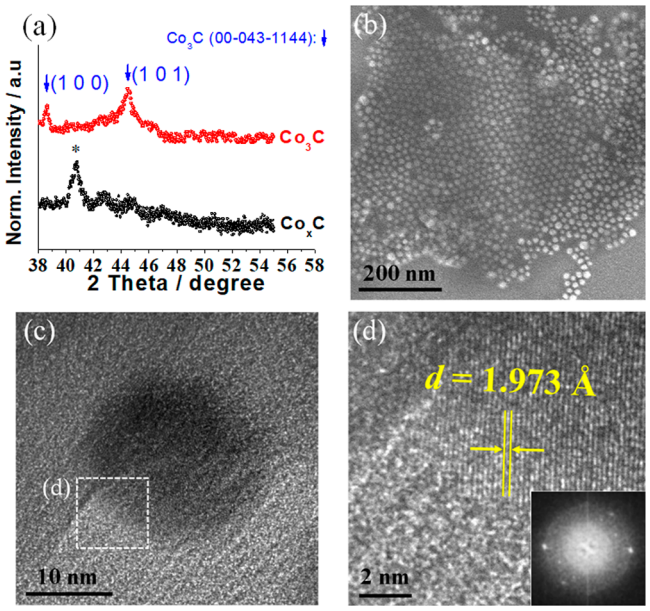

Figure 1. (a) Powder XRD patterns for as-prepared Co_xC and Co_3C. The asterisk represents organic impurities attributed to precursors. (b) Low-resolution TEM and (c) HRTEM images for Co_3C. (d) Enlarged HRTEM image which is taken from the region in the white frame in panel c. The inset in panel d shows the FFT image.

pattern changed significantly after the heat treatment. The Co_xC sample changed such that Co_3C was the dominant phase with the strongest peak at around 45° (101) and a notable peak at around 39° (100). The microscopic structure and morphology of the Co_3C were investigated using TEM, as shown in Figure 1b−d. Our Co_3C material is composed of nanostructured spherical particles with uniform sizes of 20−30 nm in diameter. In Figure 1d, the lattice fringe throughout the particle indicates the high crystallinity and single-crystalline nature of the Co_3C nanoparticle. The HRTEM image for the edge portion of the Co_3C particle indicates a lattice fringe spacing of 1.973 Å, which can be assigned to the (112) planes of cubic Co_3C (intensity profile in Figure S2).[25] The intense spots in the FFT image also confirm the single-crystalline nature of the Co_3C nanoparticle.

OER electrocatalytic performance of the Co_3C precatalyst was evaluated using rotating disk electrode (RDE) measurements, as displayed in Figure 2. Polarization curves and overpotentials (at 10 and 40 $mA{\cdot}cm^{-2}_{geo}$) for the OER for both the Co_3C precatalyst and commercial CoO samples on the basis of geometric surface area are shown in Figure 2a,b. We collected a second sweep of a linear sweep voltammetry (LSV) curve for analysis of the OER (in the range of 1.0−1.9 V) because the oxidation of the Co_3C particles occurred primarily during the first sweep (see the Figure 2a inset). The inset shows there are two distinct peaks in the anodic region; the peak in the vicinity of 0.3 V is related to the oxidation of carbide ($Co_3C \rightarrow Co_3O_4$), and Co_3O_4 is oxidized to CoOOH and/or Co_2O_3 at ∼1.2 V.[26]

One can readily see that Co_3C and CoO have similar overpotentials (455 mV) on the glassy carbon (GC) substrates at 10 $mA{\cdot}cm^{-2}_{geo}$, however Co_3C showed a lower overpotential (511 mV) than CoO (566 mV) at a higher current density (40 $mA{\cdot}cm^{-2}_{geo}$). To separate surface area effects from the intrinsic activity, we analyzed the ECSA (details in Figure S3) and computed an ECSA normalized current density (mA·

DOI: 10.1021/acsaem.8b01336
ACS Appl. Energy Mater. 2018, 1, 5145−5150

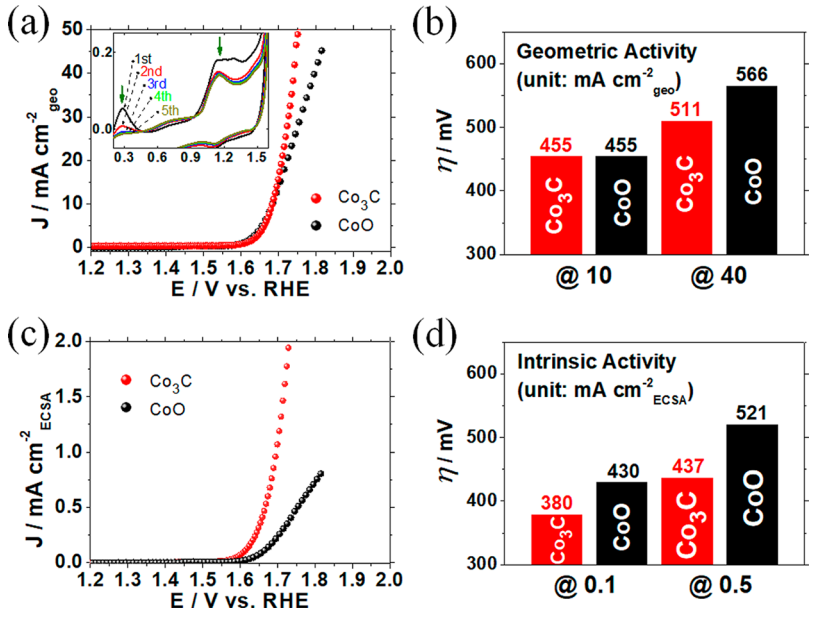

Figure 2. OER polarization curves and overpotential table of Co_3C and commercial CoO, based on (a, b) geometric electrode surface area and (c, d) ECSA, respectively. Inset: cyclic voltammograms of Co_3C with the polarization sweep numbers (first to fifth sweeps). Note that the Co_3C particle was transformed into a Co_3C–CoO_x core–shell particle in the first to second sweeps (see Figure 3).

cm$^{-2}_{ECSA}$).[27] Interestingly, the estimation of intrinsic activity shows a significant difference (at this stage) between the Co_3C precatalyst and CoO, suggesting that the Co_3C-derived electrocatalyst has a higher intrinsic activity than the CoO at both lower and higher current densities (380, 437 mV for the Co_3C and 430, 521 mV for the CoO at 0.1 and 0.5 mA·cm$^{-2}_{ECSA}$, respectively).

As illustrated in Figure 3a,b, the morphological structure of the Co_3C catalyst after two LSV sweeps retains its spherical shape during the OER testing. However, the outer surface of the post-LSV Co_3C particle has clearly changed to an amorphous structure with a thickness of ~4 nm as determined by HRTEM analysis. This structure is in contrast to the well-defined crystallinity of the Co_3C particle prior to electrochemical testing (presented in Figure 1). Lattice fringes [d = 3.016 Å, (111) plane for Co_3C[25] and intensity profile in Figure S4] were clearly confirmed in the core part of the particle, which demonstrates that Co_3C remains in the core, and the shell of the particle was transformed into an amorphous oxide after two LSV sweeps due to its exposure to the water oxidizing conditions. Further analysis of this transformation within the Co_3C particle was studied by XPS with Ar^+ sputtering, as represented in Figure 3c,d. The peak related to Co carbide at 778.4 eV significantly increased (4% at surface and 40% in bulk), while the Co oxide peak at 780.5 eV decreased (96% at surface and 60% in bulk) in the Co $2p_{3/2}$ region of the sputtered post-LSV Co_3C particle. The peak area related to the C–Co bond was also estimated in the C 1s region (see Figure S5), and the small increase in the C–Co signal after Ar^+ sputtering (11% at surface and 16% in bulk) clearly supports a core–shell structure. Due to this core–shell structure, electron conductivity in the particle could be higher in the post-LSV Co_3C (resulting in the higher slope in the OER region, Figure 2a) core–shell particle than in the commercial CoO particle for OER electrocatalysis, since Co_3C is a much better electron conductor than cobalt oxide.[29]

The formation of the oxide shell around Co_3C shows that cobalt carbide is intrinsically unstable in the oxidative

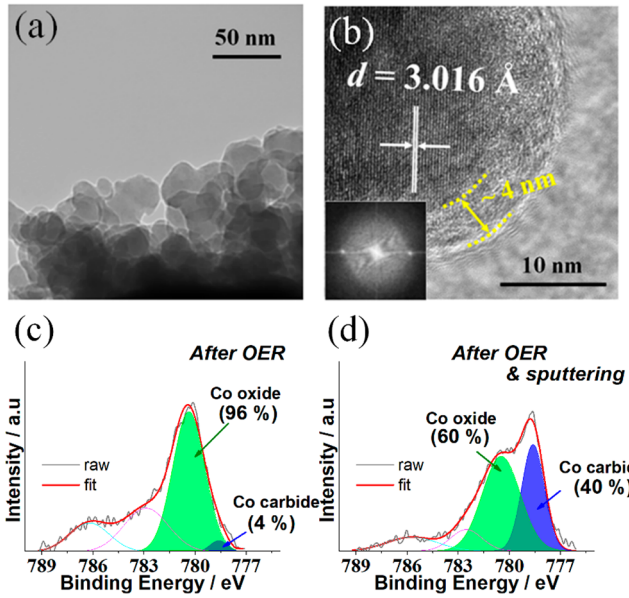

Figure 3. (a) Low-magnification TEM (bright-field) and (b) HRTEM images for Co_3C, prepared after OER testing (after second LSV). The inset in panel b shows the FFT image. XPS core level of the Co $2p_{3/2}$ region for (c) Co_3C (after OER test) and (d) Co_3C after the OER test with Ar^+ sputtering for 10 s at a rate of 0.5 nm·s^{-1}. A Shirley background was subtracted from the spectrum before deconvolution. Blue solid line, Co carbide; green line, Co oxide; pink and cyan lines, Co (oxy)hydroxide satellite peaks.[26,28]

environment present during OER testing; thus, we were motivated to further check the electrochemistry and materials characterization.[14,30] We have estimated the ECSA of the Co_3C particles after various numbers of OER LSV potential sweeps (1.0–1.9 V), as shown in Figure 4a. This data set (Figure 4a) can be separated into two major parts: before and after ~150 sweeps. The ECSA continuously increases until ~150 sweeps, which we believe to be due to gradual oxidation

DOI: 10.1021/acsaem.8b01336
ACS Appl. Energy Mater. 2018, 1, 5145–5150

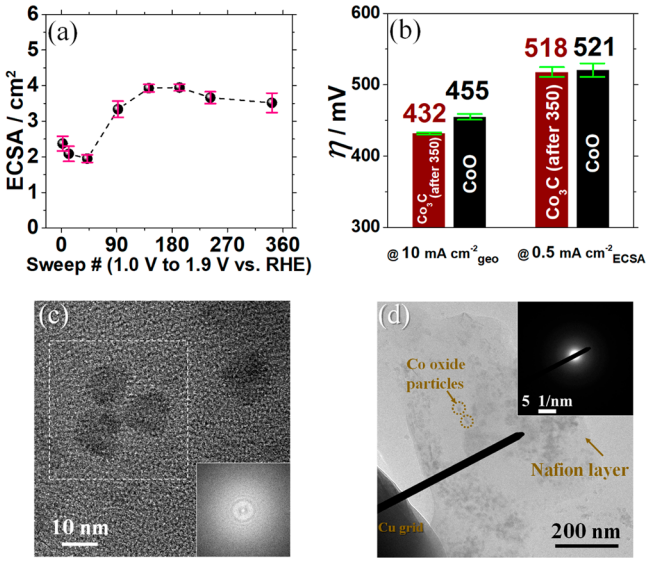

Figure 4. (a) Trend of ECSAs vs sweep number for the Co_3C sample. (b) OER activity comparison (based on geometric surface area as well as ECSA) for Co_3C (after 350 LSV OER sweeps) vs commercial CoO. (c) High-resolution and (d) bright-field TEM images for Co_3C (prepared after 350 sweeps of OER). Inset of panel c: FFTs calculated from the areas marked with white-dotted square. Inset of panel d: Corresponding selective area electron diffraction (SAED) pattern.

of cobalt from the surface to the core in the Co_3C particle. After ~150 sweeps, the ECSA value was relatively stable. Moreover, the original Co_3C particle after 150 sweeps did not possess a core–shell structure nor lattice fringes (see Figure S6). Thus, the oxidation of a Co_3C particle into an amorphous Co oxide particle is likely completed at ~150 sweeps or the rate of oxidation might have been slowed significantly. The data shown in Figure 4b indicate that although the fully oxidized Co_3C shows a higher geometric OER activity (432 mV) than the commercial CoO (455 mV), its intrinsic activity (518 mV) was very similar to that of the commercial cobalt oxide (521 mV). This result is very different from those of the Co_3C and CoO shown in Figure 2 (which were measured after only two LSV sweeps): the activity based on geometry is the same for that case (at 10 mA·cm$^{-2}_{geo}$), and the Co_3C showed better intrinsic activity. It is clear, from Figure 4c that the Co_3C particle examined after 350 OER LSV sweeps is again an amorphous oxide (also confirmed by the SAED pattern in Figure 4d and by XRD analysis in Figure S7—we believe the particle is completely transformed to oxide after 150 LSV sweeps), which is clearly different than the commercial crystalline CoO (see Figure S8). Additionally, the fully oxidized Co_3C (amorphous Co oxide) retained the original shape of the parent Co_3C particle.

Finally, to summarize the entire oxidation process of Co_3C during OER testing, the trends of OER overpotentials based on geometric electrode surface area and ECSA against sweep number are summarized in Figure 5. In stage 1, amorphous Co oxide shells were formed through the surface oxidation of Co_3C particles after two LSV sweeps. Subsequently, the further oxidation of Co_3C proceeded toward its complete oxidation until ~150 sweeps and the thicknesses of the amorphous Co oxide shells are enlarged (stage 2). In this stage, the overpotential at 10 mA·cm$^{-2}_{geo}$ gradually decreased owing to the active surface area enhancement via continuous formation of amorphous Co oxide on the outer surface (see Figure 4a).

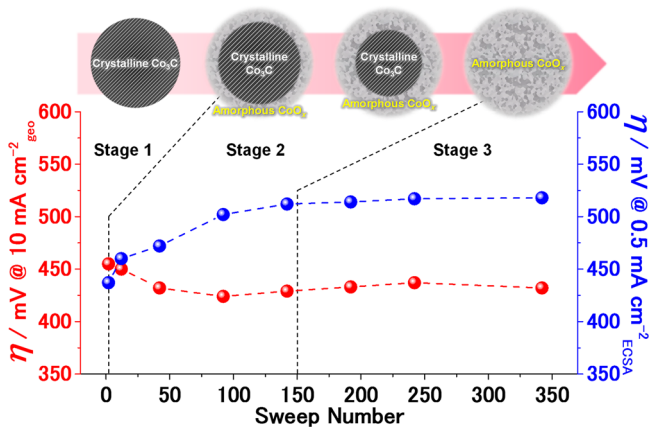

Figure 5. Trend of OER overpotentials (η) based on geometric electrode surface area (red) and ECSA (blue) vs sweep number (OER LSV sweep nos. 1.0–1.9 V vs RHE) for the Co_3C sample.

At the same time, the overpotential at 0.5 mA·cm$^{-2}_{ECSA}$ is lowered by gradual formation of amorphous Co oxide having low electron conductivity (on the conductive metal–carbide surface) which disturbs a conducting path for electrons (details in Figure S9). After the compete oxidation of Co_3C, amorphous Co oxide particles showed a low overpotential at 10 mA·cm$^{-2}_{geo}$ and a superior stability in a long-term OER testing (stage 3). In particular, the low overpotential at 10 mA·cm$^{-2}_{geo}$ was likely due to a porous nanostructure that is formed by the transformation from crystalline carbides into amorphous oxides due to the complete replacement of carbon with oxygen in the Co_3C crystallites during the long-term OER testing and allows the OER to occur within the pores of the fully oxidized particles. Taking into consideration the factors mentioned above, amorphous Co oxide is the true catalytic site for the OER, while Co_3C is a superior electron conductor that does not appear to be catalytically active itself. Furthermore, it was confirmed that the kinetic barriers to oxide transformation of Co_3C are low and the complete oxidation of Co_3C could minimize the overpotential based on geometric electrode surface area.

In conclusion, we have studied the transformation of Co_3C particles during OER testing and found that the cobalt carbide is gradually converted to an amorphous Co oxide in approximately 150 LSV sweeps and that this oxide is the true OER catalyst. We believe the transformation follows this trend: (i) crystalline Co_3C → (ii) Co_3C core–amorphous Co oxide shell → (iii) amorphous Co oxide. Surprisingly, the amorphous Co oxide particle produced from Co_3C recorded a relatively lower overpotential (432 mV) than the Co_3C–CoO_x core–shell particle (455 mV) at 10 mA·cm$^{-2}_{geo}$. This is attributed to the enlargement of the ECSA during the full oxidation of crystalline Co_3C into amorphous Co oxide, resulting in an increase in OER active sites per unit area of the electrode surface. We believe that this enlargement in active surface area is the primary origin of the improved OER activity in nanoporous Co oxide derived from the initial precatalyst material, Co_3C. We anticipate that other transition metal carbide precatalysts will evolve similarly to the cobalt carbide catalyst reported here, based on the stability of transition metal carbides in an oxidizing environment. Extrapolating further, we would expect all metal chalcogenide, carbide, and pnictide starting materials for OER electrocatalysis to be eventually fully converted to metal oxides or (oxy)hydroxides. That some

DOI: 10.1021/acsaem.8b01336
ACS Appl. Energy Mater. 2018, 1, 5145–5150

materials apparently do not oxidize (e.g., Ni_3Se_2[6,23]) is both interesting and important, meriting the further investigation of the chemical stability of other materials in this family.

■ ASSOCIATED CONTENT

Supporting Information

The Supporting Information is available free of charge on the ACS Publications website at DOI: 10.1021/acsaem.8b01336.

Experimental and characterization details as well as further analysis of the Co_3C OER electrocatalyst (PDF)

■ AUTHOR INFORMATION

Corresponding Author

*E-mail: mullins@che.utexas.edu.

ORCID

Kenta Kawashima: 0000-0001-7318-6115

Yang Liu: 0000-0002-7240-1546

C. Buddie Mullins: 0000-0003-1030-4801

Author Contributions

‖J.-H.K. and K.K. contributed equally to this work.

Notes

The authors declare no competing financial interest.

■ ACKNOWLEDGMENTS

This work was supported by the Welch Foundation through Grant F-1436, and by the National Science Foundation via Grant CHE-1664941.

■ REFERENCES

(1) Liang, Y.; Li, Y.; Wang, H.; Dai, H. Strongly Coupled Inorganic/nanocarbon Hybrid Materials for Advanced Electrocatalysis. *J. Am. Chem. Soc.* **2013**, *135*, 2013−2036.

(2) Kunze, J.; Stimming, U. Electrochemical Versus Heat-Engine Energy Technology: A Tribute to Wilhelm Ostwald's Visionary Statements. *Angew. Chem., Int. Ed.* **2009**, *48*, 9230−9237.

(3) Kanan, M. W.; Nocera, D. G. In Situ Formation of an Oxygen-Evolving Catalyst in Neutral Water Containing Phosphate and Co^{2+}. *Science* **2008**, *321*, 1072−1075.

(4) Kim, J.-H.; Shin, K.; Kawashima, K.; Youn, D. H.; Lin, J.; Hong, T. E.; Liu, Y.; Wygant, B. R.; Wang, J.; Henkelman, G.; Mullins, C. B. Enhanced Activity Promoted by CeO_x on a CoO_x Electrocatalyst for the Oxygen Evolution Reaction. *ACS Catal.* **2018**, *8*, 4257−4265.

(5) Subbaraman, R.; Tripkovic, D.; Chang, K.-C.; Strmcnik, D.; Paulikas, A. P.; Hirunsit, P.; Chan, M.; Greeley, J.; Stamenkovic, V.; Markovic, N. M. Trends in Activity for the Water Electrolyser Reactions on 3d M(Ni,Co,Fe,Mn) Hydr(oxy)oxide Catalysts. *Nat. Mater.* **2012**, *11*, 550−557.

(6) Feng, L. L.; Yu, G.; Wu, Y.; Li, G. D.; Li, H.; Sun, Y.; Asefa, T.; Chen, W.; Zou, X. High-Index Faceted Ni_3S_2 Nanosheet Arrays as Highly Active and Ultrastable Electrocatalysts for Water Splitting. *J. Am. Chem. Soc.* **2015**, *137*, 14023−14026.

(7) Qian, H.; Tang, J.; Wang, Z.; Kim, J.; Kim, J. H.; Alshehri, S. M.; Yanmaz, E.; Wang, X.; Yamauchi, Y. Synthesis of Cobalt Sulfide/Sulfur Doped Carbon Nanocomposites with Efficient Catalytic Activity in the Oxygen Evolution Reaction. *Chem. - Eur. J.* **2016**, *22*, 18259−18264.

(8) Chen, Z.; Wu, R.; Liu, M.; Liu, Y.; Xu, S.; Ha, Y.; Guo, Y.; Yu, X.; Sun, D.; Fang, F. Tunable Electronic Coupling of Cobalt Sulfide/Carbon Composites for Optimizing Oxygen Evolution Reaction Activity. *J. Mater. Chem. A* **2018**, *6*, 10304−10312.

(9) Dutta, A.; Samantara, A. K.; Dutta, S. K.; Jena, B. K.; Pradhan, N. Surface-Oxidized Dicobalt Phosphide Nanoneedles as a Nonprecious, Durable, and Efficient OER Catalyst. *ACS Energy Lett.* **2016**, *1*, 169−174.

(10) Wang, Y.; Liu, D.; Liu, Z.; Xie, C.; Huo, J.; Wang, S. Porous Cobalt−Iron Nitride Nanowires as Excellent Bifunctional Electrocatalysts for Overall Water Splitting. *Chem. Commun.* **2016**, *52*, 12614−12617.

(11) Wang, Y.; Xie, C.; Liu, D.; Huang, X.; Huo, J.; Wang, S. Nanoparticle-Stacked Porous Nickel−Iron Nitride Nanosheet: A Highly Efficient Bifunctional Electrocatalyst for Overall Water Splitting. *ACS Appl. Mater. Interfaces* **2016**, *8*, 18652−18657.

(12) Ma, T. Y.; Cao, J. L.; Jaroniec, M.; Qiao, S. Z. Interacting Carbon Nitride and Titanium Carbide Nanosheets for High-Performance Oxygen Evolution. *Angew. Chem., Int. Ed.* **2016**, *55*, 1138−1142.

(13) Rasmussen, F. A.; Thygesen, K. S. Computational 2D materials database: electronic structure of transition-metal dichalcogenides and oxides. *J. Phys. Chem. C* **2015**, *119*, 13169−13183.

(14) Jin, S. Are Metal Chalcogenides, Nitrides, and Phosphides Oxygen Evolution Catalysts or Bifunctional Catalysts? *ACS Energy Lett.* **2017**, *2*, 1937−1938.

(15) Xu, R.; Wu, R.; Shi, Y.; Zhang, J.; Zhang, B. Ni_3Se_2 Nanoforest/Ni Foam as a Hydrophilic, Metallic, and Self-supported Bifunctional Electrocatalyst for both H_2 and O_2 Generations. *Nano Energy* **2016**, *24*, 103−110.

(16) Masa, J.; Barwe, S.; Andronescu, C.; Sinev, I.; Ruff, A.; Jayaramulu, K.; Elumeeva, K.; Konkena, B.; Roldan Cuenya, B.; Schuhmann, W. Low Overpotential Water Splitting Using Cobalt−Cobalt Phosphide Nanoparticles Supported on Nickel Foam. *ACS Energy Lett.* **2016**, *1*, 1192−1198.

(17) Li, X.; Han, G. Q.; Liu, Y. R.; Dong, B.; Hu, W. H.; Shang, X.; Chai, Y. M.; Liu, C. G. NiSe@NiOOH core−shell hyacinth-like nanostructures on nickel foam synthesized by in situ electrochemical oxidation as an efficient electrocatalyst for the oxygen evolution reaction. *ACS Appl. Mater. Interfaces* **2016**, *8*, 20057−20066.

(18) Chen, P.; Xu, K.; Fang, X.; Tong, Y.; Wu, J.; Lu, X.; Peng, X.; Ding, H.; Wu, C.; Xie, Y. Metallic Co_4N Porous Nanowire Arrays Activated by Surface Oxidation as Electrocatalysts for the Oxygen Evolution Reaction. *Angew. Chem.* **2015**, *127*, 14923−14927.

(19) Chen, W.; Liu, Y. Y.; Li, Y. Z.; Sun, J.; Qiu, Y. C.; Liu, C.; Zhou, G. M.; Cui, Y. In Situ Electrochemically Derived Nanoporous Oxides from Transition Metal Dichalcogenides for Active Oxygen Evolution Catalysts. *Nano Lett.* **2016**, *16*, 7588−7596.

(20) Xu, X.; Song, F.; Hu, X. A Nickel Iron Diselenide-derived Efficient Oxygen-evolution Catalyst. *Nat. Commun.* **2016**, *7*, 12324−12330.

(21) Mabayoje, O.; Shoola, A.; Wygant, B. R.; Mullins, C. B. The Role of Anions in Metal Chalcogenide Oxygen Evolution Catalysis: Electrodeposited Thin Films of Nickel Sulfide as "Pre-catalysts". *ACS Energy Lett.* **2016**, *1*, 195−201.

(22) Kwak, I. H.; Im, H. S.; Jang, D. M.; Kim, Y. W.; Park, K.; Lim, Y. R.; Cha, E. H.; Park, J. $CoSe_2$ and $NiSe_2$ Nanocrystals as Superior Bifunctional Catalysts for Electrochemical and Photoelectrochemical Water Splitting. *ACS Appl. Mater. Interfaces* **2016**, *8*, 5327−5334.

(23) Swesi, A. T.; Masud, J.; Nath, M. Nickel Selenide as a High-efficiency Catalyst for Oxygen Evolution Reaction. *Energy Environ. Sci.* **2016**, *9*, 1771−1782.

(24) Chen, W.; Wang, H.; Li, Y.; Liu, Y.; Sun, J.; Lee, S.; Lee, J.-S.; Cui, Y. In Situ Electrochemical Oxidation Tuning of Transition Metal Disulfides to Oxides for Enhanced Water Oxidation. *ACS Cent. Sci.* **2015**, *1*, 244−251.

(25) Nagakura, S. Study of Metallic Carbides by Electron Diffraction Part IV. Cobalt Carbides. *J. Phys. Soc. Jpn.* **1961**, *16*, 1213−1219.

(26) Syugaev, A. V.; Lyalina, N. V.; Lomayeva, S. F.; Maratkanova, A. N. Electrochemical Behavior of Co_3C Carbide. *J. Solid State Electrochem.* **2015**, *19*, 2933−2941.

(27) Suntivich, J.; May, K. J.; Gasteiger, H. A.; Goodenough, J. B.; Shao-Horn, Y. A Perovskite Oxide Optimized for Oxygen Evolution Catalysis from Molecular Orbital Principles. *Science* **2011**, *334*, 1383−1385.

(28) Wang, H.; Wong, S. P.; Cheung, W. Y.; Ke, N.; Wen, G. H.; Zhang, X. X.; Kwok, R. W. M. Magnetic Properties and Structure

DOI: 10.1021/acsaem.8b01336
ACS Appl. Energy Mater. 2018, 1, 5145−5150

Evolution of Amorphous Co-C Nanocomposite Films Prepared by Pulsed Filtered Vacuum Arc Deposition. *J. Appl. Phys.* **2000**, *88*, 4919−4921.
(29) Kim, Y.-T.; Lopes, P. P.; Park, S.-A.; Lee, A. Y.; Lim, J.; Lee, H.; Back, S.; Jung, Y.; Danilovic, N.; Stamenkovic, V.; Erlebacher, J.; Snyder, J.; Markovic, N. M. Balancing Activity, Stability and Conductivity of Nanoporous Core-shell Iridium/Iridium Oxide Oxygen Evolution Catalysts. *Nat. Commun.* **2017**, *8*, 1449−1456.
(30) Shatynski, S. R. The Thermochemistry of Transition Metal Carbides. *Oxid. Met.* **1979**, *13*, 105−118.

DOI: 10.1021/acsaem.8b01336
ACS Appl. Energy Mater. 2018, 1, 5145−5150